East European Journal of Physics. 3. 443-455 (2026)
DOI:10.26565/2312-4334-2026-3-40 ISSN 2312-4334

NUMERICAL INVESTIGATION OF JEFFREY NANOFLUID OVER A MOVING THIN NEEDLE WITH EXOTHERMIC CHEMICAL REACTION: A LEVENBERG-MARQUARDT NEURAL NETWORK APPROACH

R. Krishnakumari[1#], V. Sugunamma[2##], M. Jayachandra Babu[3*], J. Girish Kumar[4]**
[1]*Department of Mathematics, Sri Venkateswara University, Tirupati, Andhra Pradesh, India – 517502*
[2]*Department of Mathematics, Sri Venkateswara University, Tirupati, Andhra Pradesh, India – 517502*
[3]*Department of Mathematics, Government Degree College, Rajampeta, Andhra Pradesh, India – 516115*
[4]*Department of Mathematics, Government Degree College, Nagari, Andhra Pradesh, India – 517590*
email: [#]krishnarun.krishna81@gmail.com; [##]vsugunar@gmail.com; [**]drjgireeshkumar@gmail.com
**Corresponding Author email: jayamacharla@gmail.com*
Received April 3, 2026; revised June 29, 2026; accepted July 3, 2026

This study examines the heat and mass transmission properties of a Jeffrey nanofluid traveling across a moving slender needle. The main aim is to examine how essential parameters, such as Hall current, couple stress, activation energy, and thermophoresis, affect the fluid's velocity, temperature, concentration, and corresponding entropy generation. The flow configuration of a slender needle is critically pertinent to practical applications, including the thermal design of microneedles for regulated medication delivery, the aerodynamic profiling of slender structural elements in aerospace engineering, and the optimization of delicate sensor probes. With the aid of suitable similarity transformations, the equations which were meant to describe the problem, were transmuted as a framework with nonlinear ordinary equations, and then solved using the bvp4c solver. A notable discovery is that fluid velocity is hindered by augmented magnetic field strength and coupling stresses, while the temperature profile is improved by elevated viscous dissipation and thermophoresis effects. Moreover, the heat transfer rate at the surface decreases as the thermophoresis parameter increases, whereas the mass transfer rate diminishes with higher activation energy. The study indicates that entropy formation, representing energy loss, increases with heightened viscous dissipation and thermal radiation. It is found that the Sherwood number declines by 24.1% when activation energy rises from 0 to 0.8. It is found that the Nusselt number declines by 26.3% when thermophoresis parameter rises from 0 to 2. It is discovered that the friction factor raises by 2.32% when magnetic field parameter escalates from 0 to 2.
Keywords: *Thermophoresis; bvp4c; Brownian motion; Couple stress; Activation energy*

Nomenclature

σ	Electrical conductivity	η	Similarity variable
u, v	Velocity components in x, y directions respectively	D_T	Thermophoresis diffusion coefficient
Pr	Prandtl number	σ^*	Stefan-Boltzmann constant
λ_0	Relaxation time parameter of the fluid	Br	Brinkman number
λ_1	Retardation parameter of the fluid	α_1	Concentration difference parameter
De	Deborah number	Ra	Thermal radiation parameter
ρ	Density	k^*	Mean absorption coefficient
α	Temperature difference parameter	g	Gravitational acceleration
Le	Lewis number	n	Fitting rate constant
C_P	Specific heat	R_0	Universal gas constant
Mg	Magnetic field Parameter	λ^*	Buoyancy parameter
γ	Exothermic/endothermic coefficient	Cs	Couple stress parameter
β_C, β_T	Concentration and thermal expansion Coefficients	D_B	Brownian motion coefficient
Nt	Thermophoresis parameter	Nb	Brownian motion parameter
k_0, Γ	Reaction rate parameters	k_1	Boltzmann constant
m	Hall current parameter	d	Needle size parameter
		E_0, A	Activation energy parameters

1 INTRODUCTION

The Buongiorno model is significant for its innovative integration of two primary nanoparticle transport mechanisms—Brownian motion and thermophoresis—within a unified continuum framework, thereby fundamentally enhancing the analysis of nanofluid heat transfer beyond the capabilities of conventional single-phase models. The significance is highlighted by its extensive use as a standard for forecasting the improved thermal properties of nanofluids, offering essential insights into the influence of nanoparticle distribution on flow dynamics and temperature distributions. This has resulted in crucial applications in the design and optimization of high-performance thermal management systems, such as microchannel coolers for electronics, solar thermal collectors, nuclear reactor safety, and advanced heat exchangers, where precise modelling of the interaction between nanoparticle migration and convective heat transfer is imperative for enhancing energy efficiency. Bhatti et al. [1] studied the entropy formation in the Eyring–Powell nanofluid

Cite as: R. Krishnakumari, V. Sugunamma, M.J. Babu, J.G. Kumar, East Eur. J. Phys. 3, 443 (2026), https://doi.org/10.26565/2312-4334-2026-3-40

traversing a porous stretching surface by using the Successive Linearization Method. The research indicated that temperature and nanoparticle concentration profiles rise with an elevated thermophoresis parameter. Amanulla et al. [2] performed an inquiry of nanofluid movement via an upward surface, integrating velocity and thermal slip effects with the Keller-Box method. The research indicated that increased velocity slip augments momentum at proximity to the surface. Goodarzi et al. [3] inspected the flow and thermal transfer characteristics of a non-Newtonian nanofluid within a microtube. The research indicated that augmenting the nanoparticle volume percentage improves heat transport within the microtube. Subba Rao et al. [4] investigated the convective flow of Casson nanofluid across an isothermal sphere under convective boundary conditions. The research indicated that a rise in the Casson parameter slows down the flow. Ahmadian et al. [5] scrutinized the movement of a Maxwell nanofluid amongst two horizontally revolving disks subjected to an axial magnetic field with the bvp4c approach. The research indicated that elevated Deborah number values diminish radial velocity while improving the temperature profile. Usman et al. [6] examined the dynamics of a bioconvective and radiative Cross nanofluid between two stretchable spinning disks employing the homotopy analysis technique. The study demonstrated that fluid velocity escalates with elevated disk stretching rate and buoyancy parameters. Elgazery [7] inspected the movement of a Powell–Eyring micropolar nanofluid over an elastic permeable framework with non-constant thermophysical parameters. The results showed that the angular velocity goes up when the variable microrotation viscosity parameter changes. This shows how important it is to characterize these kinds of features as functions instead of constants. Yousef et al. [8] studied the movement of a Casson–Williamson nanofluid via a permeable stretched sheet. It is discovered that the temperature profile is enhanced by higher values of the Casson parameter. A second-grade nanofluid's movement through an exponentially stretched framework with a variable thermal conductivity parameter was studied by Anwar et al. [9]. The velocity profile was found to be more raised with higher values of the material parameter. Furthermore, several researchers [10-16] inspected various non-Newtonian fluid movements across different frameworks.

The interaction between exothermic reaction and fluid movement is an important phenomenon that has far-reaching effects on many fields of engineering. The heat that comes out of the reaction changes the fluid's properties, like its temperature, density, and viscosity. This can then modify the flow behaviour in a big way, causing buoyancy-driven convection, speeding up flow rates, or even causing instabilities. This coupling is very important in real life because it determines how safe and efficient chemical reactors are, how stable flames are and how heat is spread in combustion systems like engines and turbines, and how to control the thermal field in materials processing, such as welding and crystal growth, to make sure the products are of high quality. To get the best performance and make sure that a wide range of thermal and chemical systems work safely, it is important to understand this synergy. Kareem et al. [17] examined the transient behaviour and entropy generation of the Rivlin-Ericksen fluid undergoing a two-step exothermic reaction with temperature-dependent viscosity. The study demonstrated that entropy generation decreased under scenarios characterized by low viscous dissipation and diminished fluid viscosity. Raees et al. [18] formed a mathematical model to study the movement of nanofluid in a microchannel with an exothermic chemical reaction parameter, based on Buongiorno's model. The findings demonstrated that the Frank-Kamenetskii parameter substantially improves heat transmission. Ahmad et al. [20] studied the mixed convective movement of an incompressible fluid through a curved surface with an exothermic catalytic chemical reaction parameter by the finite difference approach. It is found that the surge in the exothermic parameter results in an elevation of the temperature profile. Ogunsola et al. [21] conducted an irreversibility analysis for third-grade fluid movement characterized by an Arrhenius exothermic reaction and non-constant viscosity parameters. The study demonstrated that augmenting the Frank-Kamenetskii parameter amplifies entropy formation. Zainal et al. [22] scrutinized the movement of an aqueous hybrid nanofluid across a moving wedge utilizing the bvp4c solver. It is shown that augmenting the nanoparticle volume fraction improves the friction factor. Furthermore, several researchers [23-28] inspected the impact of exothermic chemical reaction on various fluid movements across different frameworks.

The fluid dynamics around a moving thin needle is a basic problem in boundary layer theory that is very useful in real life. This setup is especially useful since it makes it possible to find a similarity solution, even when the needle's thickness is about the same as the boundary layer that forms. This feature makes it a great example for checking the accuracy of numerical codes and experimental data. It has a lot of uses, from improving the aerodynamic performance of thin structural parts and hypersonic vehicle nose cones to making medical devices like microneedles and surgical tools better, where precise control of fluid drags and heat transmission is very important. Waini et al. [29] scrutinized the movement of a hybrid nanofluid past a moving thin needle. The study indicated that dual solutions arise within particular intervals of the moving parameter. Kumar et al. [30] inspected the movement of a Casson fluid past a moving slender needle with cross-diffusion effects. The study showed that there is a decline in the Nusselt number with the rise in the Dufour number. Ramesh et al. [31] examined the movement of a bioconvective hybrid nanofluid via a moving slender needle, utilizing a modified Buongiorno's model. Abbas et al. [32] conducted a theoretical analysis of the movement of a hybrid nanofluid past a moving slender needle employing the Galerkin method. The study demonstrated that increased needle thickness reduces the heat transmission rate. Later, Srinivasa Reddy [33] discussed the fluid movement through the moving slender needle.

Although the current literature offers considerable understanding of nanofluid flows across diverse geometries, a notable research gap persists in the thorough examination of a Jeffrey nanofluid traversing a moving thin needle, which concurrently integrates the combined influences of Hall current, couple stresses, and an Arrhenius activation energy-driven exothermic reaction. This study is significant as it addresses the existing gap by creating a comprehensive model that encapsulates the intricate interactions of electromagnetic, microstructural, and chemical kinetic phenomena, which are crucial for the precise design of advanced micro-devices and high-precision engineering systems. Additionally, to enhance the dependability of our numerical computations derived from the bvp4c solver, an Artificial Neural Network (ANN) model is utilized to corroborate essential results. This machine learning methodology offers independent validation of our results and illustrates the powerful synergy between numerical analysis and data-driven modelling in contemporary computational fluid dynamics, thereby augmenting the credibility and robustness of the research presented.

2. MATHEMATICAL FORMULATION

In this study, the steady movement of a Jeffrey nanofluid over a moving thin needle is considered.

(i) The fluid is characterized as a non-Newtonian Jeffrey fluid. This model integrates relaxation time effects, rendering it appropriate for viscoelastic fluids.
(ii) A vertical external magnetic field with strength B is applied. The model incorporates the influence of Hall current (parameter m), which alters the Lorentz force exerted on the fluid (refer to Fig. 1).
(iii) The microstructure of the fluid is taken into account by adding couple stress effects to the momentum equation. This takes into account how particles interact in microfluids and adds a higher-order derivative term.
(iv) The model integrates Brownian motion and thermophoresis, which are essential for the behaviour of nanofluids.
(v) It is assumed that the needle moves with a constant velocity U_w in the same or opposite direction to the mainstream of constant velocity U_∞.
(vi) The chemical reaction is assumed to be exothermic, meaning that it releases heat ($\gamma > 0$). This assumption is crucial for analyzing the thermal effects of the reaction on the fluid flow.
(vii) This formulation is based on the idea that the needle is very thin. This thin needle approach assumes that the needle's diameter is very small relative to the thickness of the boundary layer that is forming. As a result, the flow field and the heat and mass transfer processes that go along with it are thought to be unaffected by the needle's limited radius or blunt tip. This means that the specified similarity transformations and boundary conditions can be used.

Based on the assumptions made before, this investigation requires the following conditions and equations (Ishak et al. [34], Ashraf et al. [35], and Karthik et al. [36]):

$$\frac{\partial}{\partial r}(vr)+\frac{\partial}{\partial x}(ur)=0 \tag{1}$$

$$\begin{aligned}\frac{\partial u}{\partial x}u+\frac{\partial u}{\partial r}v&=\frac{\upsilon}{1+\lambda_0}\left[\frac{\partial^2 u}{\partial r^2}+\frac{1}{r}\frac{\partial u}{\partial r}+\lambda_1\left(\frac{\partial u}{\partial r}\frac{\partial^2 u}{\partial x\partial r}+u\frac{\partial^3 u}{\partial x\partial r^2}+\frac{\partial v}{\partial r}\frac{\partial^2 u}{\partial r^2}+\frac{u}{r}\frac{\partial^2 u}{\partial x\partial r}+v\frac{\partial^3 u}{\partial r^3}+\frac{v}{r}\frac{\partial^2 u}{\partial r^2}\right)\right]\\&-\left(\sigma u B^2\right)\frac{1}{\rho\left(1+m^2\right)}-\frac{1}{\rho}\left(\frac{\partial^4 u}{\partial r^4}+\frac{2}{r}\frac{\partial^3 u}{\partial r^3}-\frac{1}{r^2}\frac{\partial^2 u}{\partial r^2}+\frac{1}{r^3}\frac{\partial u}{\partial r}\right)\gamma_0+\beta_C\left(C_w-C_\infty\right)g+\beta_T\left(T_w-T_\infty\right)g\end{aligned} \tag{2}$$

$$\begin{aligned}v\frac{\partial T}{\partial r}+u\frac{\partial T}{\partial x}&=\left(\left(k+\frac{16}{3}\frac{\sigma * T_\infty^3}{k *}\right)\left(\frac{\partial^2 T}{\partial r^2}+\frac{1}{r}\frac{\partial T}{\partial r}\right)\right)\frac{1}{(\rho C_p)}+\frac{1}{(\rho C_p)}\frac{\sigma B^2}{1+m^2}u^2\\&+\frac{\gamma\rho k_0}{\rho C_p}\exp\left(-\frac{E_0}{k_B T}\right)\left(\frac{T}{T_\infty}\right)^n(C-C_\infty)+\tau\left(D_B\frac{\partial T}{\partial r}\frac{\partial C}{\partial r}+\frac{D_T}{T_\infty}\left(\frac{\partial T}{\partial r}\right)^2\right)+\frac{\mu}{(\rho C_p)}\left(\frac{\partial u}{\partial r}\right)^2.\end{aligned} \tag{3}$$

$$v\frac{\partial C}{\partial r}+u\frac{\partial C}{\partial x}=D_B\left(\frac{\partial^2 C}{\partial r^2}+\frac{1}{r}\frac{\partial C}{\partial r}\right)+\frac{D_T}{T_\infty}\left(\frac{\partial^2 T}{\partial r^2}+\frac{1}{r}\frac{\partial T}{\partial r}\right)-k_0\exp\left(-\frac{E_0}{k_B T}\right)\left(\frac{T}{T_\infty}\right)^n(C-C_\infty) \tag{4}$$

$$\left.\begin{aligned}&\text{at } r=R(x): u=U_w, C=C_w, \frac{\partial^2 u}{\partial r^2}=0, v=0, T=T_w,\\&\text{as } r\to\infty: T\to T_\infty, \frac{\partial u}{\partial r}\to 0, C\to C_\infty, u\to U_\infty.\end{aligned}\right\} \tag{5}$$

Here $r=R(x)$ is the surface shape of the needle.

For the purpose of converting governing equations, Ishak et al. [34] introduced the following similarity transformations:

$$\left.\eta=\frac{Ur^2}{\upsilon x}, v=-\frac{\upsilon}{r}(f-\eta f'), \phi(\eta)=\frac{C-C_\infty}{C_w-C_\infty}, u=2Uf', \theta(\eta)=\frac{T-T_\infty}{T_w-T_\infty}.\right\} \tag{6}$$

Note that U is the composite velocity which is equal to U_w+U_∞.

By substituting $\eta=d$ in $\eta=\frac{Ur^2}{\upsilon x}$, we can get $R(x)=\sqrt{\frac{\upsilon d x}{U}}$.

The terms shown in (6) easily satisfy the equation (1). The following outcome results from the effective modification of equations (2-4) and conditions in (5) by the use of integration of (6):

$$\frac{1}{1+\lambda_0}\left(2\eta f''' + f'' - De\left(2\eta f''^2 + 6\eta f' f''' + 4f' f'' + 4\eta f f'''' + 6 f f'''\right)\right) - \frac{Mg}{1+m^2} f' - 32\eta^2 Cs f''''' - Cs(104\eta f'''' + 34 f''') + \frac{\lambda_0}{4}(\theta + \lambda^*\phi) + f f'' = 0 \tag{7}$$

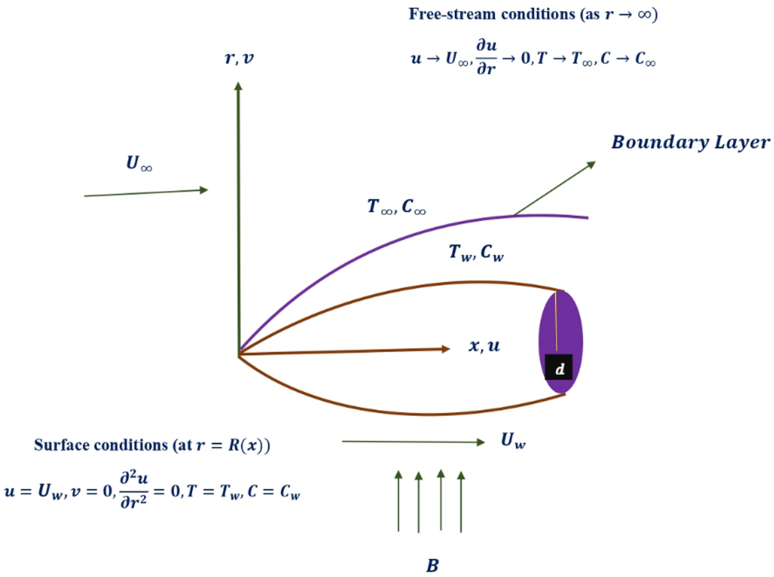

Figure 1. Visual representation of the present investigation

$$\frac{1+Ra}{\Pr}(\theta' + \eta\theta'') + \frac{2}{1+m^2} Mg Eck f'^2 + \frac{f\theta'}{2} + (Nb\theta'\phi' + Nt\theta'^2)\eta + \frac{\chi\Gamma}{4}(1+\alpha\theta)^n \exp\left(-\frac{A}{1+\alpha\theta}\right)\phi + 4\eta Eck f''^2 = 0 \tag{8}$$

$$\frac{2}{Le}(\phi' + \eta\phi'') + \frac{2}{Le}\frac{Nt}{Nb}(\theta' + \eta\theta'') + f\phi' - \frac{\Gamma}{2}(1+\alpha\theta)^n \exp\left(-\frac{A}{1+\alpha\theta}\right)\phi = 0 \tag{9}$$

$$\left.\begin{array}{l} \text{at } \eta = d: f(\eta) = \frac{1}{2}d\lambda, \phi(\eta) = 1, f'(\eta) = \frac{1}{2}\lambda, \theta(\eta) = 1, f'''(\eta) = 0, \\ \text{as } \eta \to \infty: f'(\eta) \to \frac{1}{2}(1-\lambda), \theta(\eta) \to 0, f''(\eta) \to 0, \phi(\eta) \to 0. \end{array}\right\} \tag{10}$$

Note that we assumed that $0 < \lambda < 1$ i.e., the needle and the fluid move in the same direction (positive $x-$ direction).

$$\left.\begin{array}{c} Mg = \frac{\sigma_f B_0^2}{\rho U}, B = \frac{B_0}{\sqrt{x}}, De = U\lambda_2, \lambda_2 = \frac{\lambda_1}{x}, Cs = \frac{\gamma_1 U}{\rho \upsilon^2}, \gamma_1 = \frac{\gamma_0}{x}, Le = \frac{\upsilon}{D_B}, \\ Ra = \frac{16}{3}\frac{\sigma * T_\infty^3}{kk *}, \lambda^* = \frac{Gc}{Gr}, \lambda_0 = \frac{Gr}{\mathrm{Re}_x^2}, Gr = \frac{g\beta_T(T_w - T_\infty)}{\upsilon^2}, \mathrm{Re}_x = \frac{Ux}{\upsilon}, \\ \Pr = \frac{\mu C_p}{k}, \chi = \frac{\gamma(C_w - C_\infty)}{C_p(T_w - T_\infty)}, \Gamma = \frac{k_2}{U}, k_2 = \frac{k_0}{\sqrt{x}}, A = \frac{E_0}{k_B T_\infty}, \lambda = \frac{U_w}{U}, \\ \alpha = \frac{T_w - T_\infty}{T_\infty}, Nb = \frac{\tau D_B(C_w - C_\infty)}{\upsilon}, Eck = \frac{U^2}{C_p(T_w - T_\infty)}, Nt = \frac{\tau D_T(T_w - T_\infty)}{\upsilon T_\infty}. \end{array}\right\}$$

The friction factor can be stated via the ensuing equation:

$$Cf = \frac{1}{\rho}\left(\frac{\partial u}{\partial r}\right)\frac{\mu}{U^2}\bigg|_{r=R(x)} \tag{11}$$

By applying (6), term in (11) can be rewritten as:

$$\sqrt{\mathrm{Re}_x}\, Cf = 4\sqrt{\eta}\, f''(\eta)\Big|_{\eta=d}.$$

The following formulas can be used to determine the heat and mass transfer rates:

$$Nu = \left.\frac{-xq_w}{k_f\left(T_w - T_\infty\right)}\right|_{r=R(x)}, q_w = \left(k + \frac{4}{3}\frac{4\sigma^* T_\infty^3}{k^*}\right)\frac{\partial T}{\partial r},$$
$$Sh = \left.\frac{-x}{\left(C_w - C_\infty\right)}\frac{s_w}{D_m}\right|_{r=R(x)}, s_w = D_m\frac{\partial C}{\partial r}. \quad (12)$$

By applying (6), the formulas in (12) are rewritten as:

$$\left(\mathrm{Re}_x\right)^{-1/2} Nu = -2\sqrt{\eta}\left(1+Ra\right)\theta'(\eta)\Big|_{\eta=d},$$
$$\left(\mathrm{Re}_x\right)^{-1/2} Sh = -2\sqrt{\eta}\phi'(\eta)\Big|_{\eta=d}.$$

2.1. Entropy generation

The formula that describes the dimensional computation of entropy production is mentioned as:

$$S_g = \left(1 + 16\frac{\sigma^* T_\infty^3}{3k_f k^*}\right)\left(\frac{k_f}{T_\infty^2}\right)\left(\frac{\partial T}{\partial r}\right)^2 + \mu\frac{1}{T_\infty}\left(\frac{\partial u}{\partial r}\right)^2 + \sigma\frac{1}{T_\infty}u^2B^2 + \frac{1}{C_\infty}\left(\frac{\partial C}{\partial r}\right)^2 R_0 D_m + \frac{1}{T_\infty}\frac{\partial C}{\partial r}\frac{\partial T}{\partial r}R_0 D_m \quad (13)$$

By adopting (6), we may rewrite equation (13) as follows:

$$N_{EG} = \left(1+Ra\right)\alpha\eta\theta'^2 + 4Br\eta f''^2 + 2Brf'^2 Mg + H\frac{\alpha_1}{\alpha}\phi'^2 + H\theta'\phi',$$

where

$$\alpha_1 = \frac{C_w - C_\infty}{C_\infty},\ Br = \frac{\mu_f U^2}{\left(T_w - T_\infty\right)k_f},\ N_{EG} = \frac{\upsilon T_\infty x S_g}{4U\left(T_w - T_\infty\right)k_f},\ H = \frac{R_0\left(C_w - C_\infty\right)D_m}{k_f}.$$

3. NUMERICAL PROCEDURE

The equations (7) to (9), together with the conditions specified in (10), are solved using the bvp4c solver. Prior beginning coding, it is essential to contemplate the subsequent assumptions.

$$f = \psi_1, f' = \psi_2, f'' = \psi_3, f''' = \psi_4, f^{iv} = \psi_5, \theta = \psi_6, \theta' = \psi_7, \phi = \psi_8, \phi' = \psi_9.$$

This system of first-order ordinary differential equations is generated from equations (7) to (9) and the conditions outlined in (10).

$$\psi_1' = \psi_2,$$
$$\psi_2' = \psi_3,$$
$$\psi_3' = \psi_4,$$
$$\psi_4' = \psi_5,$$
$$\psi_5' = \frac{1}{32}\frac{1}{\eta^2}\frac{1}{Cs}\left[\begin{array}{c}\frac{1}{1+\lambda_0}\left(2\eta\psi_4 + 2\psi_3 - De(2\eta\psi_3{}^2 + 6\eta\psi_2\psi_4 + 4\psi_2\psi_3 + 4\eta\psi_1\psi_5 + 6\psi_1\psi_4)\right) \\ -\frac{Mg}{1+m^2}\psi_2 - Cs(104\eta\psi_5 + 34\psi_4) + \frac{\lambda}{4}(\psi_6 + \lambda^*\psi_8) + \psi_1\psi_3\end{array}\right],$$
$$\psi_6' = \psi_7,$$
$$\psi_7' = \frac{-\Pr}{\eta(1+Ra)}\left[\begin{array}{c}\frac{1+Ra}{\Pr}\psi_7 + \frac{2}{1+m^2}MgEck\psi_2{}^2 + \frac{\psi_1\psi_7}{2} + (Nb\psi_7\psi_9 + Nt\psi_7{}^2)\eta \\ +\frac{\chi\Gamma}{4}(1+\alpha\psi_6)^n\exp\left(-\frac{A}{1+\alpha\psi_6}\right)\psi_8\end{array}\right],$$
$$\psi_8' = \psi_9,$$
$$\psi_9' = \frac{-Le}{2\eta}\left[\frac{2}{Le}\frac{Nt}{Nb}(\psi_7 + \eta\psi_7') + \psi_1\psi_9 - \frac{\Gamma}{2}(1+\alpha\psi_6)^n\exp\left(-\frac{A}{1+\alpha\psi_6}\right)\psi_8 + \frac{2}{Le}\psi_9\right]. \quad (15)$$

with the constraints

$$\left.\begin{array}{l}\psi a(1)=\frac{1}{2}d\lambda,\psi a(4)=0,\psi a(6)=1,\psi a(8)=1,\psi a(2)=\frac{1}{2}\lambda,\\ \psi b(2)=\frac{1}{2}(1-\lambda),\psi b(3)=0,\psi b(6)=0,\psi b(8)=0.\end{array}\right\} \tag{16}$$

The graphical results can be generated by executing the code once the system has been constructed in MATLAB.

4. ANALYSIS OF THE RESULTS

Analysis of Fig. 2 reveals that an elevation in De correlates with a decrease in the velocity of the fluid. An elevated De value indicates that the fluid demonstrates more significant elastic solid-like characteristics over an extended period, as opposed to solely viscous liquid-like behavior. As elasticity gets more pronounced, the fluid's internal resistance to deformation escalates, hindering its motion and leading to a diminished overall velocity profile. This conclusion indicates that increased fluid elasticity creates a more robust resistance mechanism in the flow, hence inhibiting momentum diffusion and diminishing the kinetic energy available for fluid motion. According to the data presented in Fig. 3, an elevation in Cs is associated with a reduction in the fluid's velocity. The couple stress parameter reflects the impact of internal rotational resistance and micro-rotational effects in the fluid, resulting from the suspension of micro-elements such as polymers or colloidal particles. An increased value of this characteristic indicates enhanced resistance to fluid movement and deformation caused by these microstructures. This indicates that the fluid becomes significantly more viscous or organized, hindering its capacity to flow freely. As a result, the velocity profile is diminished due to increased energy dissipation required to counteract internal coupling tensions, resulting in an overall slowdown of the flow.

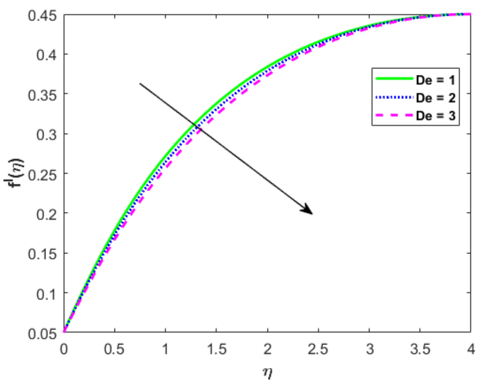

Figure 2. De's impact on fluid's velocity

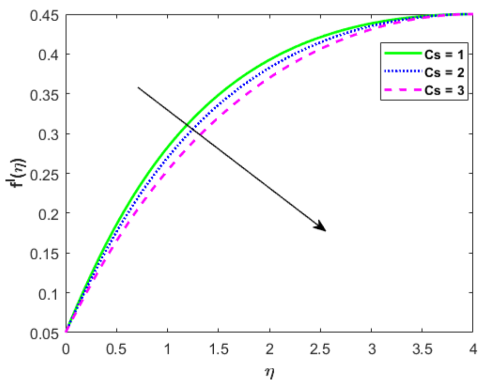

Figure 3. Cs's impact on fluid's velocity

Fig. 4 explains that the fluid temperature upsurges with increased Eckert number values. An increased Eckert number indicates that a substantial fraction of the fluid's kinetic energy is transformed into internal thermal energy due to work performed against viscous forces. This study suggests that in high-velocity flows or very viscous fluids, frictional heating becomes a predominant factor, resulting in a significant temperature increase without requiring an external heat source. Fig. 5 establishes that the temperature of the fluid rises with higher thermophoresis parameter values.

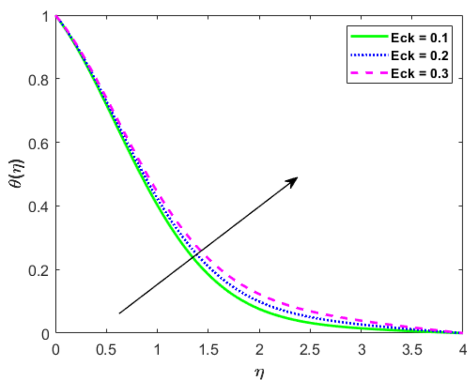

Figure 4. Eck's impact on fluid's temperature

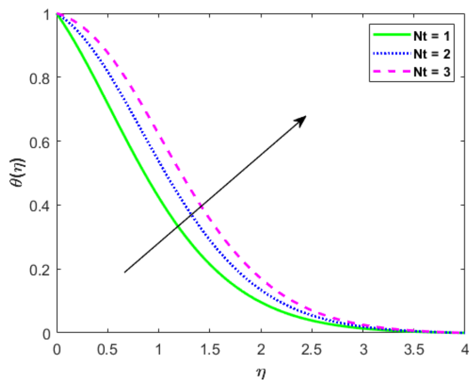

Figure 5. Nt's impact on fluid's temperature

Thermophoresis is a phenomenon in which microscopic particles, such as those in a colloidal suspension or nanofluid, are subjected to a force that propels them from a hotter region to a colder one. An elevation in the thermophoresis parameter amplifies the movement of particles away from the heated surface. As a result, an increased quantity of particles congregates in the colder areas of the fluid, hence augmenting energy transfer and thermal conduction in that area. This result indicates that thermophoresis serves as a crucial mechanism for energy redistribution, effectively raising the overall fluid temperature by concentrating heat-carrying particles within the bulk fluid, thus impacting the system's thermal management and efficiency. Fig. 6 demonstrates that an elevation in the Brownian motion parameter correlates with a reduction in nanoparticle concentration within the fluid. This occurs physically due to the amplification of Brownian motion, which exacerbates the erratic, chaotic movement of nanoparticles. This intensified microscopic motion breaks the homogeneous distribution of particles, facilitating their dispersion and preventing their settling or accumulation. As a result, the total concentration of nanoparticles in the primary fluid domain diminishes due to their enhanced scattering. This outcome underscores the pivotal function of Brownian diffusion as a counteracting force to concentration accumulation, accentuating its significance in regulating particle distribution in fields such as nano-fluidics and thermal systems. Fig. 7 illustrates that an elevation in the activation energy parameter leads to an increased fluid concentration. A higher activation energy signifies a more substantial energy barrier that reactant molecules must surmount to engage in the chemical reaction. As a result, the reaction rate is diminished, resulting in decreased consumption of reactant species. As fewer molecules undergo transformation, the concentration of the fluid rises due to the accumulation of reactants. This finding indicates that activation energy functions as a kinetic inhibitor; in practical systems such as industrial reactors or biological processes, elevated activation energy retards chemical conversion, thereby enabling a greater concentration of the initial substances to remain in the fluid medium.

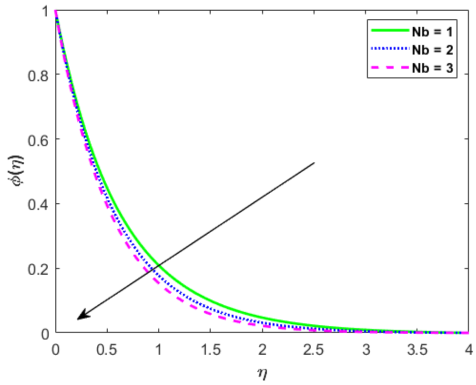

Figure 6. Nb's impact on fluid's concentration

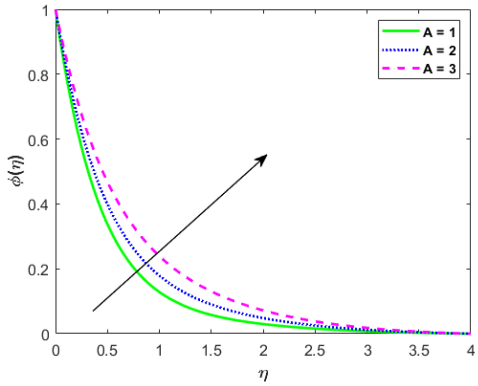

Figure 7. A's impact on fluid's concentration

Table 1 demonstrates that a spike in Cs elevates the skin friction coefficient. This is because as elevated pair stresses amplify the internal resistance to fluid microrotation, thereby raising the shear stress at the surface. This indicates a more robust contact between the fluid's microstructure and the boundary, leading to increased frictional drag. The observed rise in skin friction coefficient with a greater magnetic field, seen in Table 1, is a direct result of the magnetic influence on fluid flow. Physically, this occurs because the applied magnetic field causes a resistive force that opposes the direction of fluid motion. This force impedes the flow, making the fluid more resistant to shearing at the surface. As a result, friction factor increases. It is discovered that the friction factor raises by 2.32% when Mg escalates from 0 to 2.

Table 1. Influence of Mg and Cs on Cf

Mg	Cs	Skin friction coefficient
0		0.340707
0.5		0.352124
1		0.363684
1.5		0.37539
2		0.387244
	0.1	0.778157
	0.6	0.897543
	1.1	0.91059
	1.6	0.915594
	2.1	0.91824

Table 2 demonstrates that an elevation in the Eckert number correlates with a reduction in the Nusselt number. An elevated Eck indicates that the energy lost due to fluid friction becomes increasingly prominent relative to the heat transmitted via conduction. Physically, this indicates that as viscous forces increase, they produce internal heat within the fluid flow. This self-generated heat functions as an internal source, elevating the temperature of the fluid and diminishing the temperature gradient between the surface and the bulk fluid. Consequently, the Nusselt number diminishes. Table 2 demonstrates that an increase in the thermophoresis parameter leads to a reduction in the Nusselt number. A more potent thermophoretic force propels a greater number of nanoparticles away from the heated surface and into the core fluid region. As a result, a diminished concentration of particles develops along the boundary, serving as an insulating layer and diminishing the temperature difference at the wall. The physical implication is that the heat transfer rate from the surface is reduced, as the thermophoresis process generates thermal resistance by displacing suspended particles that would otherwise facilitate energy flow. It is found that the Nusselt number declines by 26.3% when Nt rises from 0 to 2.

Table 2 Influence of Eck and Nt on Nu

Eck	Nt	Nusselt number
0		0.89449
0.1		0.87495
0.2		0.855375
0.3		0.835792
0.4		0.816202
	0	1.052693
	0.5	0.892532
	1	0.752287
	1.5	0.630638
	2	0.526129

According to the trend shown in Table 3, a rise in the activation energy parameter is linked to a drop in the Sherwood number. This happens because a larger activation energy means that reactant molecules have to overcome a bigger energy barrier for the chemical reaction to happen. As a result, the reaction rate slows down, which means that the reactants at the surface are used up more slowly. The slower chemical kinetics cause the lower mass transfer rate, which is immediately reflected in the lower Sherwood number. This means that mass transfer happens less quickly when the chemical process that controls it is more sensitive to heat and needs a lot more energy to start. Table 3 shows that there is an inverse relationship between the Brownian motion parameter and the Sherwood number. This means that when nanoparticles move about more randomly, it can slow down the total mass transfer rate. The physical explanation for this phenomenon is that vigorous Brownian diffusion results in nanoparticles dispersing more randomly throughout the fluid bulk, instead of being moved in a synchronized fashion towards the surface. This chaotic motion disturbs the directed concentration gradient that is necessary for effective convective mass transfer. This causes the Sherwood number, which measures this mass transfer efficiency, to go down. It is found that the Sherwood number declines by 24.1% when A rises from 0 to 0.8.

Table 3 Influence of A and Nb on Sh

A	Nb	Sherwood number
0		1.836886
0.2		1.776357
0.4		1.723082
0.6		1.676444
0.8		1.635843
	0.1	2.117563
	0.6	1.587075
	1.1	1.528717
	1.6	1.501083
	2.1	1.482726

Fig. 8 displays that as the Brinkman number goes up, the rate of entropy formation in the fluid flow goes up as well. This happens because the Brinkman number is the ratio of the heat generated by viscous dissipation to the heat moved by molecular conduction. A higher Brinkman number means that the heat transmission through conduction is less important than the heat transfer through friction. This increased viscous dissipation results in heightened thermal irreversibilities, which serve as a direct source of entropy. The physical implication is that in flows with high viscous effects, such as those involving very viscous fluids or high speeds, the energy losses due to friction are more significant, leading to a more irreversible and thermodynamically less efficient system. Fig. 9 illustrates that as the thermal radiation parameter goes up, the rate of entropy creation in the fluid flow also goes up.

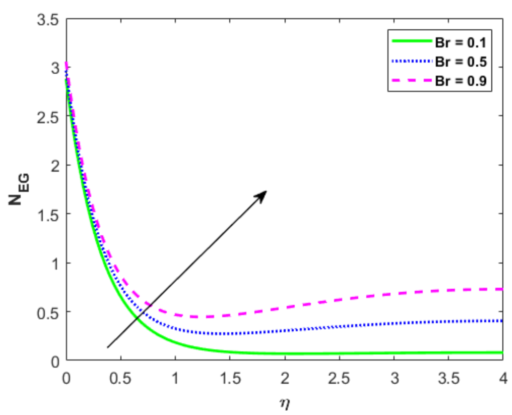

Figure 8. Br's impact on N_{EG}

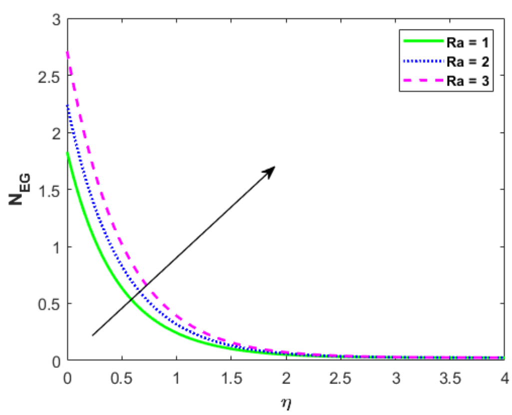

Figure 9. Ra's impact on N_{EG}

This happens because more thermal radiation makes the energy transfer and the thermal gradients in the system stronger. This result means that the system is less efficient from a thermodynamic point of view. The higher entropy generation means that more useful energy is lost, which means that more energy is wasted as heat instead of being used for productive activity. This lowers the system's overall performance.

4.1. Validation of the results using Levenberg-Marquardt algorithm

To independently validate our numerical results, an Artificial Neural Network (ANN) model was developed using the Levenberg-Marquardt (LM) backpropagation algorithm. The network architecture consisted of a three-layer feedforward structure: an input layer, a single hidden layer, and an output layer. The input layer received the parameter values (magnetic field parameter Mg for friction factor predictions; thermophoresis parameter Nt for Nusselt number predictions; and reaction rate parameter A for Sherwood number predictions). The hidden layer comprised 10 neurons with the hyperbolic tangent sigmoid (tansig) activation function, which was selected for its ability to model nonlinear relationships effectively. The output layer employed a linear (purelin) activation function to produce the continuous target predictions. The network was trained using the Levenberg-Marquardt algorithm, which combines the advantages of the Gauss-Newton method and gradient descent, ensuring rapid convergence and enhanced stability. The dataset was randomly partitioned into three subsets: 70% for training, 15% for validation, and 15% for testing. Training was terminated when the validation error ceased to decrease for six consecutive epochs (early stopping) to prevent overfitting. The performance of the trained network was evaluated using the Mean Squared Error (MSE) and the coefficient of determination (R^2). The consistently low MSE values (ranging from 10^{-9} to 10^{-12}) and the excellent agreement between predicted and target values in the function fit plots (see Figs. 11, 13, 15) confirm the robustness and accuracy of the ANN model in capturing the underlying physical trends.

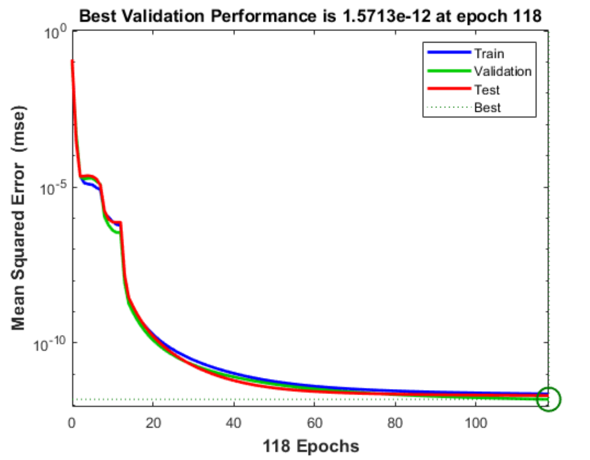

Figure 10. Mean square error plot for the outcomes related to the values of friction factor when magnetic field parameter is applied

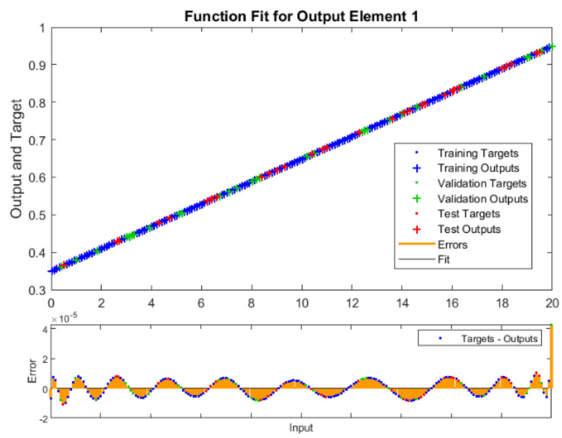

Figure 11. Function fit plot for the outcomes related to the values of friction factor when magnetic field parameter is applied

As the number of epochs becomes up, Fig. 10 shows that the mean squared error (MSE) drops quickly across training, validation, and test datasets. At first, the MSE is rather high, but it declines quickly in the first 20 epochs, which shows that learning is going quickly. As training goes on, the errors for all datasets get very close together, and by epoch 118, the best validation performance is about 1.5713×10^{-12}, which is very close to zero MSE. In Fig. 11, almost all of the outputs from training, validation, and testing are very close to their targets, following the ideal diagonal. The lower subplot backs this up by showing that the error values, which are the differences between the actual and anticipated outputs, are always close to zero across the entire input range, with no bias or systematic mistake. As the number of epochs increases, the error values for the training, validation, and test sets get closer together. This is shown in the Fig. 12, which demonstrates a steady drop MSE during neural network training. At first, the MSE lowers quickly, and then it drops more slowly over the course of 696 epochs. The model learns and generalizes the underlying pattern in the data well, as shown by the best validation accuracy at epoch 696, which has a MSE of about 1.7817×10^{-9}, which is very low. Fig. 13 displays that the neural network model's predicted values are quite near to the actual targets in the training, validation, and test datasets. All of the output points line up quite closely with the reference curve, showing that the model's predictions and the true values match very well. The error distribution in the lower subplot stays very modest across the whole input range, suggesting no consistent biases and confirming that the model well captures the underlying functional connection. Fig. 14 shows how well the neural network did over 922 training epochs. The MSE quickly went down for the training, validation, and test datasets. After a sharp drop at first, the three curves keep going down consistently until they all meet at a very low MSE. The best validation result, which was about 5.9451×10^{-11} at epoch 922, is the best of the three. The function fit plot in Fig. 15 shows that the predicted and actual values are quite close to each other in all three phases: training, validation, and testing. The data points for each subset closely match the reference fit line, which means that the model accurately represents the underlying relationship without much variance. In addition, the lower error subplot shows small residuals that are equally spread about zero, which shows that the neural network's predictions are consistently accurate and do not have any systematic mistake. Table 4 presents the Mean Squared Error (MSE), Mean Absolute Error (MAE), and coefficient of determination (R^2) for all three output variables. The exceptionally high R^2 values and the extremely low MSE and MAE values confirm that the ANN model accurately reproduces the bvp4c results with negligible error.

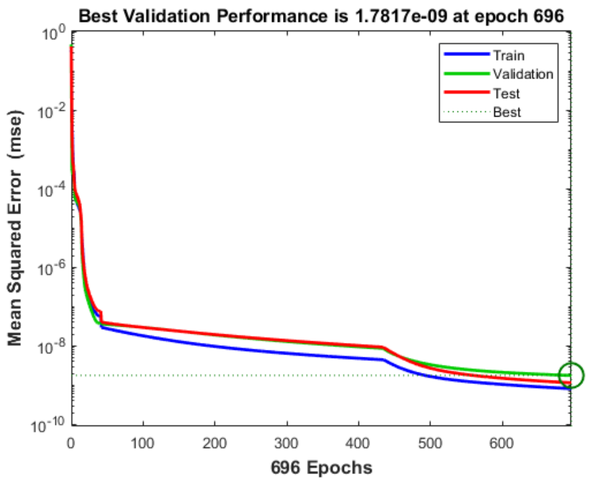

Figure 12. Mean square error plot for the outcomes related to the values of Nusselt number when thermophoresis parameter is applied

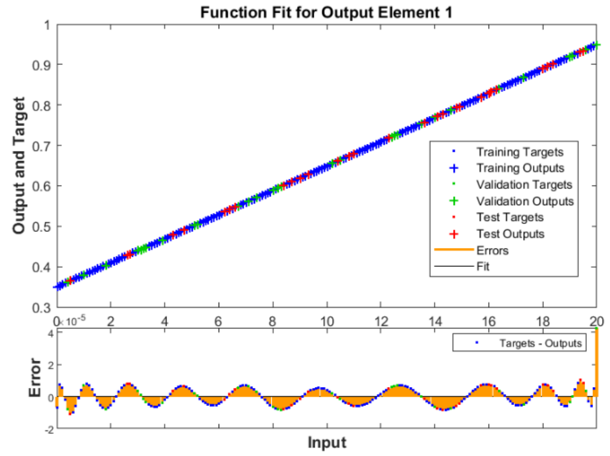

Figure 13. Function fit plot for the outcomes related to the values of Nusselt number when thermophoresis parameter is applied

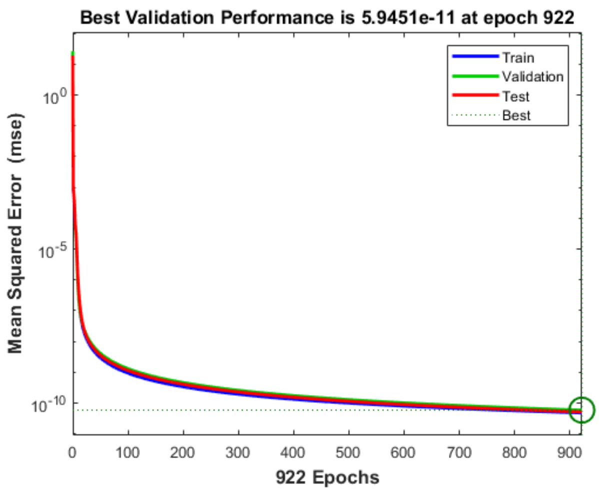

Figure 14. Mean square error plot for the outcomes related to the values of Sherwood number when reaction rate parameter is applied

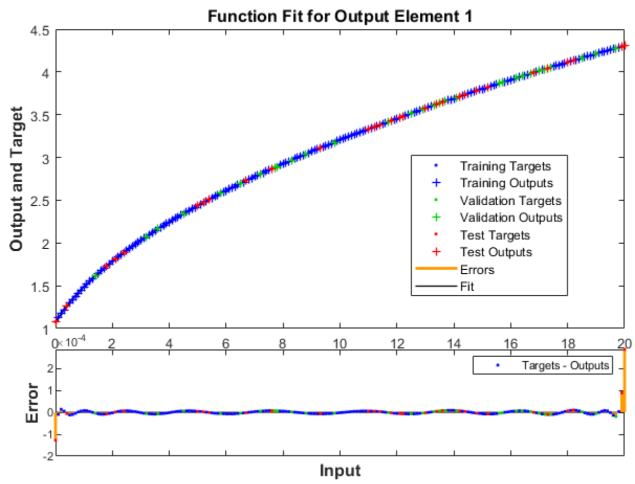

Figure 15. Function fit plot for the outcomes related to the values of Sherwood number when reaction rate parameter is applied

Table 4. Performance metrics of the Levenberg-Maquardt neural network predictions against bvp4c numerical solutions for skin friction coefficient (Cf), Nusselt number (Nu), and Sherwood number (Sh).

Output	Parameter	MSE (Mean Squared Error)	MAE (Mean Absolute Error)	R^2 (Coefficient of determination)
Cf	Mg	1.57×10^{-12}	1.02×10^{-6}	0.9999999
Nu	Nt	1.78×10^{-9}	3.85×10^{-5}	0.9999998
Sh	Γ	5.95×10^{-11}	6.52×10^{-6}	0.9999999

5. VALIDATION OF THE RESULTS

The trustworthiness of the current findings is confirmed through comparison with other investigations conducted under analogous conditions. Table 5 indicates a significant level of concordance. Table 6 represents the maximum residuals for each d value. Based on this rigorous analysis, we confirm the numerical stability of the bvp4c solver for all η values.

Table 5. Corroboration with previous outcomes for $f''(d)$

d	$f''(d)$		
	Ishak e et al. [34]	Chen and Smith [37]	Current findings
0. 1	1.2888	1.28881	1.288801329
0.01	8.4924	8.49244	8.492484394
0.001	62.1637	62.16372	62.16370642

Table 6. Numerical stability test for varying needle size parameter d: Skin friction coefficient, Nusselt number, Sherwood number, and maximum residual.

d	Skin friction coefficient	Nusselt number	Sherwood number	Maximum error
0.1	0.029086129	0.093361789	0.091683359	2.14×10^{-9}
0.05	0.065083233	0.208786501	0.205018698	2.11×10^{-9}
0.01	0.092120731	0.295309815	0.289955225	2.11×10^{-9}
0.005	0.207419712	0.661078402	0.648629831	1.96×10^{-9}
0.001	0.295923465	0.936261268	0.91778579	1.82×10^{-9}

6. CONCLUSIONS

This study has meticulously analysed the intricate transport phenomena of a Jeffrey nanofluid flow adjacent to a moving slender needle. The mathematical model was specifically designed to incorporate the collective influences of Hall current, couple stresses, temperature-dependent activation energy, and nanoparticle behaviour through Brownian motion and thermophoresis. This work is significant due to its comprehensive approach to modelling a complex and realistic system, offering essential insights that can directly improve thermal management and control strategies in micro-scale devices, advanced manufacturing, and aerospace technologies involving electromagnetic fields and chemical reactions. The key findings of the investigation, along with their physical implications, are summarized as follows:

- The fluid's velocity profile is significantly diminished by an increase in the couple stress parameter. This verifies that the internal micro-rotational resistance functions as an effective flow control mechanism, augmenting the drag force on the moving surface.
- The fluid temperature was shown to increase markedly with a rise in the Eckert number and the thermophoresis parameter. This highlights the primary influence of frictional heating and the movement of nanoparticles from warmer to cooler areas in the redistribution of thermal energy, which can be utilized to enhance uniform heating or may result in excessive overheating.
- The concentration of nanoparticles rises with elevated activation energy but diminishes with an accelerated reaction rate. This underscores that chemical reaction kinetics are a fundamental determinant of species distribution; elevated activation energy functions as a kinetic barrier, maintaining reactant concentration, whereas a rapid reaction diminishes it.
- The rates of heat and mass transfer at the needle's surface decrease with increased thermophoresis and Brownian motion parameters, respectively. This indicates a potential trade-off, wherein the mechanisms that improve bulk thermal conductivity (nanoparticle mobility) may concurrently diminish transfer efficiency at the boundary by modifying the near-wall gradients.
- The rate of entropy formation increases with elevated Brinkman and thermal radiation factors. This indicates that systems characterized by high viscous dissipation or substantial radiative heat transfer experience increased energy losses and diminished thermodynamic efficiency, a crucial factor for sustainable system design.

ORCID

M. Jayachandra Babu, https://orcid.org/0000-0001-7645-6301

REFERENCES

[1] Bhatti, M. M., Abbas, T., & Rashidi, M. M. "Entropy generation as a practical tool of optimisation for non-Newtonian nanofluid flow through a permeable stretching surface using SLM," Journal of Computational Design and Engineering, **4**(1), 21-28 (2017). https://doi.org/10.1016/j.jcde.2016.08.004

[2] Amanulla, C. H., Nagendra, N., & Reddy, M. S. "Numerical simulations on magnetohydrodynamic non-Newtonian nanofluid flow over a semi-infinite vertical surface with slipeffects," Journal of Nanofluids, **7**(4), 718-730 (2018). https://doi.org/10.1166/jon.2018.1499

[3] Goodarzi, M., Javid, S., Sajadifar, A., Nojoomizadeh, M., Motaharipour, S. H., Bach, Q. V., & Karimipour, A. "Slip velocity and temperature jump of a non-Newtonian nanofluid, aqueous solution of carboxy-methyl cellulose/aluminum oxide nanoparticles, through a microtube," International Journal of Numerical Methods for Heat & Fluid Flow, **29**(5), 1606-1628 (2019). https://doi.org/10.1108/hff-05-2018-0192

[4] Rao, A. S., Sainath, S., Rajendra, P., & Ramu, G. "Mathematical modelling of hydromagnetic casson non-Newtonian nanofluid convection slip flow from an isothermal sphere," Nonlinear engineering, **8**(1), 645-660 (2019). https://doi.org/10.1515/nleng-2018-0016

[5] Ahmadian, A., Bilal, M., Khan, M. A., & Asjad, M. I. "The non-Newtonian maxwell nanofluid flow between two parallel rotating disks under the effects of magnetic field," Scientific Reports, **10**(1), 17088 (2020). https://doi.org/10.1038/s41598-020-74096-8

[6] Usman, A. H., Khan, N. S., Humphries, U. W., Shah, Z., Kumam, P., Khan, W., ... & Ullah, Z. "Development of dynamic model and analytical analysis for the diffusion of different species in non-Newtonian nanofluid swirling flow," Frontiers in Physics, **8**, 616790 (2021). https://doi.org/10.3389/fphy.2020.616790
[7] Elgazery, N. S. "CPSM simulation of the variable properties' role in MHD non-Newtonian micropolar nanofluid flow over a stretching porous sheet (flow filtration)," Arabian Journal for Science and Engineering, **46**(8), 7661-7680 (2021). https://doi.org/10.1007/s13369-021-05489-8
[8] Yousef, N. S., Megahed, A. M., Ghoneim, N. I., Elsafi, M., & Fares, E. "Chemical reaction impact on MHD dissipative Casson-Williamson nanofluid flow over a slippery stretching sheet through porous medium," Alexandria Engineering Journal, **61**(12), 10161-10170 (2022). https://doi.org/10.1016/j.aej.2022.03.032
[9] Anwar, M. I., Firdous, H., Zubaidi, A. A., Abbas, N., & Nadeem, S. "Computational analysis of induced magnetohydrodynamic non-Newtonian nanofluid flow over nonlinear stretching sheet," Progress in reaction kinetics and mechanism, **47**, 14686783211072712 (2022). https://doi.org/10.1177/14686783211072712
[10] Sharma, B. K., Kumar, A., Gandhi, R., Bhatti, M. M., & Mishra, N. K. "Entropy generation and thermal radiation analysis of EMHD Jeffrey nanofluid flow: Applications in solar energy," Nanomaterials, **13**(3), 544 (2023). https://doi.org/10.3390/nano13030544
[11] Ashraf, M. B., Tanveer, A., & Ulhaq, S. "Effects of Cattaneo-Christov heat flux on MHD Jeffery nano fluid flow past a stretching cylinder," Journal of Magnetism and Magnetic Materials, **565**, 170154 (2023). https://doi.org/10.1016/j.jmmm.2022.170154
[12] Zeeshan, A., Khalid, N., Ellahi, R., Khan, M. I., & Alamri, S. Z. "Analysis of nonlinear complex heat transfer MHD flow of Jeffrey nanofluid over an exponentially stretching sheet via three phase artificial intelligence and Machine Learning techniques," Chaos, Solitons & Fractals, **189**, 115600 (2024). https://doi.org/10.1016/j.chaos.2024.115600
[13] Albaqami, N. N. "Using artificial neural network analysis to study Jeffrey nanofluid flow in cone–disk systems," Mathematical and Computational Applications, **29**(6), 98 (2024). https://doi.org/10.3390/mca29060098
[14] Madan Kumar, R., Srinivasa Raju, R., Kumar, M. A., & Venkateswarlu, B. "A numerical study of thermal and diffusion effects on MHD Jeffrey fluid flow over a porous stretching sheet with activation energy," Numerical Heat Transfer, Part A: Applications, **86**(13), 4423-4444 (2025). https://doi.org/10.1080/10407782.2024.2319344
[15] Butt, A. S., Anjum, A., Saeed, U. E. Z., Al Suliman, N., Alarfaj, K. K., & Souayeh, B. "Parametric Analysis of Entropy Generation in Jeffrey Nanofluid Flow Over an Exponentially Stretchable Surface with Convective Boundary Conditions and Magnetic Field Effects," Journal of Nonlinear Mathematical Physics, **32**(1), 85 (2025). https://doi.org/10.1007/s44198-025-00334-0
[16] Upadhya, S. M., Jayachandra Babu, M., & Srinivasa Babu, K. S. "Machine Learning-Enhanced Simulation of Maxwell Nanofluid Flow: A Bayesian Neural Network Approach with Thermal Relaxation and Variable Viscosity Effects," Journal of Applied and Computational Mechanics, 12(3), 815-827 (2025). https://doi.org/10.22055/jacm.2025.48495.5275
[17] Kareem, R. A., Salawu, S. O., & Yan, Y. "Analysis of transient Rivlin-Ericksen fluid and irreversibility of exothermic reactive hydromagnetic variable viscosity," J. Appl. Comput. Mech., **6**(1), 26-36 (2020). https://doi.org/10.22055/jacm.2019.28216.1460
[18] Salawu, O. "Transient analysis of radiative hydromagnetic poiseuille fluid flow of two-step exothermic chemical reaction through a porous channel with convective cooling," Journal of Computational & Applied Research in Mechanical Engineering (JCARME), **10**(1), 51-62 (2020). https://doi.org/10.22061/jcarme.2019.3986.1473
[19] Raees, A., Raees-ul-Haq, M., & Mansoor, M. "Modeling and simulations of Buongiorno's model for nanofluid in a microchannel with electro-osmotic effects and an exothermal chemical reaction," Nanomaterials, **11**(4), 905 (2021). https://doi.org/10.3390/nano11040905
[20] Ahmad, U., Ashraf, M., Abbas, A., Rashad, A. M., & Nabwey, H. A. "Mixed convection flow along a curved surface in the presence of exothermic catalytic chemical reaction," Scientific reports, **11**(1), 12907 (2021). https://doi.org/10.1038/s41598-021-92409-3
[21] Ogunsola, A. W., Oderinu, R. A., & Ohaegbue, A. D. "Entropy generation in a third-grade hydromagnetic fluid of generalised Arrhenius two-step exothermic reaction with convective cooling," International Journal of Ambient Energy, **43**(1), 8792-8801 (2022). https://doi.org/10.1080/01430750.2022.2102071
[22] Zainal, N. A., Nazar, R., Naganthran, K., & Pop, I. "Flow and heat transfer over a permeable moving wedge in a hybrid nanofluid with activation energy and binary chemical reaction," International Journal of Numerical Methods for Heat & Fluid Flow, **32**(5), 1686-1705 (2022). https://doi.org/10.1108/hff-04-2021-0298
[23] Ganesh, N. V., Al-Mdallal, Q. M., Kalaivanan, R., & Reena, K. "Arrhenius kinetics driven nonlinear mixed convection flow of Casson liquid over a stretching surface in a Darcian porous medium," Heliyon, **9**(6), (2023). https://doi.org/10.1016/j.heliyon.2023.e16135
[24] Hamza, M. M., Abdulsalam, S., & Ahmad, S. K. "Time-Dependent Magnetohydrodynamic (MHD) Flow of an Exothermic Arrhenius Fluid in a Vertical Channel with Convective Boundary Condition," Advances in Mathematical Physics, **2023**(1), 7173925 (2023). https://doi.org/10.1155/2023/7173925
[25] Das, T. K., Paul, A., & Nath, J. M. "Endo/exothermic analysis of Casson and Maxwell quadra hybrid nanofluid flow configured by pollutant concentration with thermal and solute jump," Journal of Taibah University for Science, **18**(1), 2382940 (2024). https://doi.org/10.1080/16583655.2024.2382940
[26] Khan, I., Chinyoka, T., Zulkifli, R., Muhammad, T., & Shaaban, A. A. "Computational study of non-Newtonian electro-osmotic flow between micro-parallel plates subject to Joule heating and exothermic reactions," Colloid and Polymer Science, **302**(6), 939-954 (2024). https://doi.org/10.1007/s00396-024-05242-1
[27] Ullah, I. "Activation energy with exothermic/endothermic reaction and Coriolis force effects on magnetized nanomaterials flow through Darcy–Forchheimer porous space with variable features," Waves in random and complex media, **35**(1), 398-411 (2025). https://doi.org/10.1080/17455030.2021.2023779
[28] Xin, X., Khan, I., M. Alqahtani, A., Chinyoka, T., Alroobaea, R., Zulkifli, R., & Ahmad, Z. "Numerical simulations of third-grade fluid flow with exothermic reactions in porous media-saturated vertical microchannels," Numerical Heat Transfer, Part B: Fundamentals, **86**(8), 2473-2493 (2025). https://doi.org/10.1080/10407790.2024.2345508

[29] Waini, I., Ishak, A., & Pop, I. "Hybrid nanofluid flow past a permeable moving thin needle," Mathematics, **8**(4), 612 (2020). https://doi.org/10.3390/math8040612
[30] Kumar, R. N., Gowda, R. P., Madhukesh, J. K., Prasannakumara, B. C., & Ramesh, G. K. "Impact of thermophoretic particle deposition on heat and mass transfer across the dynamics of Casson fluid flow over a moving thin needle," Physica Scripta, **96**(7), 075210 (2021). https://doi.org/10.1088/1402-4896/abf802
[31] Ramesh, G. K., Madhukesh, J. K., Aly, E. H., & Pop, I. "Modified Buongiorno's model for biomagnetic hybrid nanoliquid past a permeable moving thin needle," International Journal of Numerical Methods for Heat & Fluid Flow, **32**(11), 3551-3578 (2022). https://doi.org/10.1108/hff-10-2021-0696
[32] Abbas, Z., Rehman, A. U., Khaliq, S., & Rafiq, M. Y. "Flow dynamics of MHD hybrid nanofluid past a moving thin needle with a temporal stability test: a Galerkin method approach," Numerical Heat Transfer, Part B: Fundamentals, **84**(3), 329-347 (2023). https://doi.org/10.1080/10407790.2023.2202882
[33] Srinivasa Reddy, V., Kandasamy, J., & Sivanandam, S. "Joule heating, Dufour and Soret effects on MHD hybrid nanoliquid flow over a moving thin needle in a porous medium with thermal radiation," World Journal of Engineering, **22**(4), 866-875 (2025). https://doi.org/10.1108/wje-01-2024-0040
[34] Ishak, A., Nazar, R., & Pop, I. "Boundary Layer Flow over a Continuously Moving Thin Needle ina Parallel Free Stream," Chinese Physics Letters, **24**(10), 2895 (2007). https://doi.org/10.1088/0256-307x/24/10/051
[35] Ashraf, M. B., Tanveer, A., & Ulhaq, S. "Effects of Cattaneo-Christov heat flux on MHD Jeffery nano fluid flow past a stretching cylinder," Journal of Magnetism and Magnetic Materials, **565**, 170154 (2023). https://doi.org/10.1016/j.jmmm.2022.170154
[36] Karthik, K., Srilatha, P., Madhukesh, J. K., Khan, U., Prasannakumara, B. C., Kumar, R., ... & Abdou, M. M. M. "Computational examination of heat and mass transfer of nanofluid flow across an inclined cylinder with endothermic/exothermic chemical reaction," Case Studies in Thermal Engineering, **57**, 104336 (2024). https://doi.org/10.1016/j.csite.2024.104336
[37] Chen, J. L. S., & Smith, T. N. "Forced convection heat transfer from nonisothermal thin needles, **100**(2), 358-362 (1978). https://doi.org/10.1115/1.3450809

ЧИСЛОВЕ ДОСЛІДЖЕННЯ НАНОРІДИНИ ДЖЕФФРІ НАД РУХОМОЮ ТОНКОЮ ГОЛКОЮ З ЕКЗОТЕРМІЧНОЮ ХІМІЧНОЮ РЕАКЦІЄЮ: ПІДХІД ЛЕВЕНБЕРГА-МАРКВАРДТА НА ОСНОВІ НЕЙРОМЕРЕЖІ

Р. Крішнакумарі[1], В. Сугунамма[2], М. Джаячандра Бабу[3], Дж. Гіріш Кумар[4]
[1]*Кафедра математики, Університет Шрі Венкатешвара, Тірупаті, Андхра-Прадеш, Індія – 517502*
[2]*Кафедра математики, Університет Шрі Венкатешвара, Тірупаті, Андхра-Прадеш, Індія – 517502*
[3]*Кафедра математики, Урядовий коледж, Раджампета, Андхра-Прадеш, Індія – 516115*
[4]*Кафедра математики, Урядовий коледж, Нагарі, Андхра-Прадеш, Індія – 517590*

У цьому дослідженні розглядаються властивості тепло- та масопередачі нанорідини Джеффрі, що рухається по тонкій рухомій голці. Головна мета полягає у дослідженні того, як важливі параметри, такі як струм Холла, напруга зв'язку, енергія активації та термофорез, впливають на швидкість, температуру, концентрацію рідини та відповідне генерування ентропії. Конфігурація потоку тонкої голки має критичне значення для практичних застосувань, включаючи теплове проектування мікроголок для регульованої доставки ліків, аеродинамічне профілювання тонких структурних елементів в аерокосмічній техніці та оптимізацію чутливих сенсорних зондів. За допомогою відповідних перетворень подібності рівняння, які мали описувати проблему, були перетворені на структуру нелінійних звичайних рівнянь, а потім розв'язані за допомогою розв'язувача bvp4c. Помітним відкриттям є те, що швидкість рідини гальмується збільшеною напруженістю магнітного поля та напругами зв'язку, тоді як температурний профіль покращується завдяки підвищеній в'язкій дисипації та ефектам термофорезу. Крім того, швидкість теплопередачі на поверхні зменшується зі збільшенням параметра термофорезу, тоді як швидкість масопередачі — зі збільшенням енергії активації. Дослідження показує, що утворення ентропії, що представляє втрату енергії, зростає зі збільшенням в'язкої дисипації та теплового випромінювання. Виявлено, що число Шервуда зменшується на 24,1% зі збільшенням енергії активації від 0 до 0,8. Виявлено, що число Нуссельта зменшується на 26,3% зі збільшенням параметра термофорезу від 0 до 2. Виявлено, що коефіцієнт тертя зростає на 2,32% при збільшенні параметра магнітного поля від 0 до 2.
Ключові слова: *термофорез; bvp4c; броунівський рух; парне напруження; енергія активації*